International Journal of Bioprinting

RESEARCH ARTICLE

Osteoconductivity of bone substitutes with filament-based microarchitectures: Influence of directionality, filament dimension, and distance

Julien Guerrero[1], Chafik Ghayor[1], Indranil Bhattacharya[1], Franz E. Weber[1,2]*

[1]Center of Dental Medicine, Oral Biotechnology & Bioengineering, University of Zurich, 8032 Zurich, Switzerland

[2]CABMM, Center for Applied Biotechnology and Molecular Medicine, University of Zurich, 8057 Zurich, Switzerland

(This article belongs to the *Special Issue: 3D Printing in Tissue Engineering*)

Abstract

Additive manufacturing can be applied to produce personalized bone substitutes. At present, the major three-dimensional (3D) printing methodology relies on filament extrusion. In bioprinting, the extruded filament consists mainly of hydrogels, in which growth factors and cells are embedded. In this study, we used a lithography-based 3D printing methodology to mimic filament-based microarchitectures by varying the filament dimension and the distance between the filaments. In the first set of scaffolds, all filaments were aligned toward bone ingrowth direction. In a second set of scaffolds, which were derived from the identical microarchitecture but tilted by 90°, only 50% of the filaments were in line with the bone ingrowth direction. Testing of all tricalcium phosphate-based constructs for osteoconduction and bone regeneration was performed in a rabbit calvarial defect model. The results revealed that if all filaments are in line with the direction of bone ingrowth, filament size and distance (0.40–1.25 mm) had no significant influence on defect bridging. However, with 50% of filaments aligned, osteoconductivity declined significantly with an increase in filament dimension and distance. Therefore, for filament-based 3D- or bio-printed bone substitutes, the distance between the filaments should be 0.40 to 0.50 mm irrespective of the direction of bone ingrowth or up to 0.83 mm if perfectly aligned to it.

Keywords: Cranioplasty; Three-dimensional printing; Additive manufacturing; Polyether-ether-ketone; Fused filament fabrication

***Corresponding author:**
Franz E. Weber
(franz.weber@zzm.uzh.ch)

Citation: Guerrero J, Ghayor C, Bhattacharya I, *et al*., 2023, Osteoconductivity of bone substitutes with filament-based microarchitectures: Influence of directionality, filament dimension, and distance. *Int J Bioprint*, 9(1): 626. https://doi.org/10.18063/ijb.v9i1.626

Received: June 01, 2022
Accepted: September 21, 2022
Published Online: October 27, 2022

1. Introduction

Additive manufacturing, in contrast to subtractive methodologies, creates object layer-by-layer and allows the production of objects with so far unreached designs, particularly their microarchitecture. Microarchitecture describes the distribution of the material in the macroarchitecture. The latter is the overall shape of the object and in context of personalized bone substitutes, it matches exactly the missing piece of the patient's bone[1]. Nanoarchitecture, as third level of architecture, is characterized by the surface morphology and microporosity in the material phase, both mainly but not

exclusively dependent on the post-processing procedure[2]. Stereolithography, selective laser sintering[4], and three-dimensional (3D) printing in a powder bed[5] represent 3D printing technologies developed over the last decades[3] to build bone substitutes from ceramics[6,7].

Due to the porous structure of cancellous bone, which still is, if autologous, the gold standard bone substitute used in the clinic, the porosity and pore size were initially the main determinants for the ideal microarchitecture of synthetic bone substitutes[8]. Early studies defined rather small pore diameters to be ideal for bone substitutes[9-11]. Next, these numbers were elevated based on work with random pore-based microarchitectures in bone substitutes formed by leaching[12]. More recently, with the aid of additive manufacturing, the ideal pore diameter for osteoconductivity in pore-based scaffolds was increased from 0.80 to 1.20 mm in diameter[13].

Osteoconduction is a 3D process induced by a scaffold placed in a bone defect. The porous scaffold serves in this constellation as guiding cue for sprouting capillaries, perivascular tissue, and osteoprogenitor cells to direct them from the defect margins into the 3D structure (adjusted from[14,15]) to accelerate the bridging of the defect with bony tissue[1]. Mesenchymal stem cells are the key players during bone regeneration. Their guiding by biophysical and biochemical cues triggered by the microenvironment, which might also affect osteoconduction, has been reviewed recently[16]. Any cell guiding which enforces a directional migration of cells is a process that involves cell adhesion, polarization, and movement into a predefined direction[17-19]. The most prominent technologies to generate various types of micro/nano-structured surfaces or substrates include soft lithography, nanolithography (e.g., writing with an e-beam or dip pen), and electrospinning[20]. The so-generated features are, however, in the submicron and low micrometer range and therefore are much finer and on a lower level of dimension than the filaments used to build extrusion-based bone substitutes with diameters from low-hundreds to thousand micrometers[21]. On the cellular level of *in vitro* methodologies, it has been shown that the directionality of fibers from electrospun samples in the range of 100 nm to 1000 nm guide cell migration[22]. However, information on the effect of filaments in the 100 µm to 1000 µm range on osteoconductivity and bony bridging is scarce. The first study comparing different orientations of the laydown patterns of filaments to form a scaffold showed that *in vivo* the scaffold with the orientation of the layers of filaments at 0°/90° performed better in terms of bone formation than the counterpart in which the filaments of the layers followed the pattern 0°/60°/120°[23]. Since all these filaments were stacked in layers, all of these filaments are in the direction of bone regeneration. Unfortunately, the so-formed pores were 0.30 mm in diameter and therefore suboptimal for osteoconduction[1].

Extrusion-based additive manufacturing methodologies are widely available and frequently used because of the low cost of such systems. Melt-extrusion additive manufacturing was established in 1992[24] and solution/slurry/gel extrusion in 2002[25,26]. The latter has been widely used in bioprinting since gel extrusion allows the embedding of cells and growth factors in the extruded hydrogels. In fused deposition systems based on poly-e-caprolactone[27,28] and systems with nozzle-extruded polymers, the so-produced filaments are deposited layer-by-layer on a building platform. The variability of the microarchitecture of filament-based methodologies is, however, limited, since it depends on the dimension and the mechanical constrain predefined by the material, shape, and diameter of the filament at the time point of extrusion[1,29].

Here, we used a lithography-based additive manufacturing system for ceramics and mimicked filament-based microarchitectures with filaments between 0.40 and 1.25 mm to study the effect of filament size and distance on osteoconductivity and bone regeneration. Moreover, we compared two types of scaffolds, which were derived from the same microarchitecture in a rabbit non-critical calvarial defect model, and studied the influence of the directionality of the filament for osteoconduction. For the first type (Fil), all filaments are aligned with the natural advancement of bone in a calvarial defect. For the second type (FilG), only 50% of the filaments are aligned with the advancement of bone and the other 50% are orthogonal to it. Based on this library of eight distinct filament-based scaffolds from tri-calcium phosphate (TCP), we evaluated the effect of filament directionality, dimension, and distance on osteoconductivity and bone regeneration.

2. Materials and methods

2.1. Library of scaffolds

The scaffolds were assembled by unit cells of cubes of 0.80, 1.00, 1.75, or 2.50 mm in length to build filament-based scaffolds mimicking filaments of 0.40 mm, 0.50 mm, 0.83 mm, or 1.25 mm in square (Figure 1).

The TCP scaffolds were produced with TCP slurry LithaBone™ TCP 300 (Lithoz, Vienna, Austria)[30] using a CeraFab 7500 system (Lithoz, Vienna, Austria). The green body was assembled from 25-µm layers of slurry solidified by exposure to blue LED light at a resolution of 50-µm in the *x*/*y*-plane. The green body was removed from the building platform of the printer with a razor blade, cleaned with LithaSol 20™ (Lithoz, Vienna, Austria) and pressurized air. The polymeric binder was decomposed by heat and the

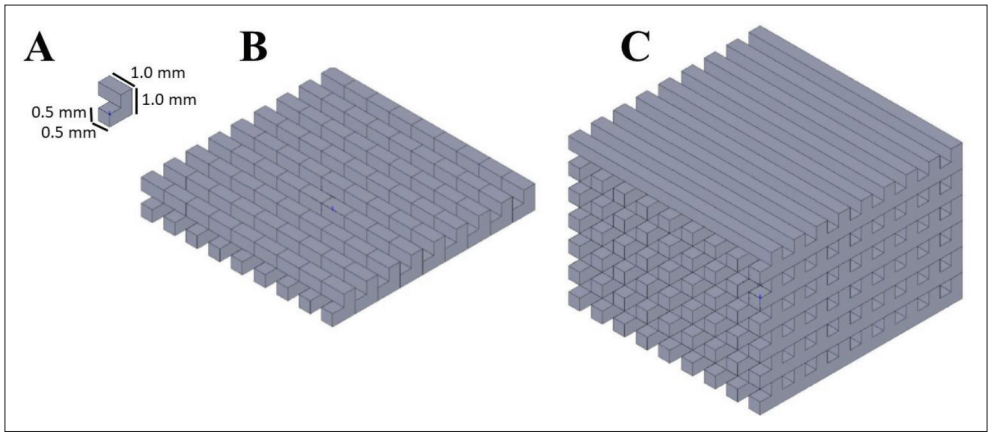

Figure 1. Construction of scaffold from the unit cell to microarchitecture. (A) A unit cell exemplified for filaments of 0.5 mm is patterned (B) and stacked (C) to form the filament-based microarchitecture.

remaining ceramic particles were sintered to increase the density with a dwell time of 3 h at 1100°C.

2.2. Surgical procedure

Eighteen (6–8 months old) female New Zealand White rabbits were used to examine the osteoconductivity of filament-based scaffolds from this library. Animals were either treated with Fil-type or FilG-type implants using a calvarial defect model[2]. The protocol was in line with the European Union Directive 2010/63/EU and accepted by the local authorities (065/2018). In brief, animals were anesthetized before surgery by injection of 65 mg/kg ketamine and 4 mg/kg xylazine and maintained during the operation with a mix of isoflurane and O_2. Next, the skin on top the cranium was disinfected and an incision was made from the nasal bone to the mid-sagittal crest. After the soft tissue was deflected and fixed, the periosteum was removed. By the use of a 6-mm trephine bur, four defects were marked. Inside this mark, all defects were completed with rose burrs of 5 mm in diameter, followed by a burr with a 1 mm diameter to preserve the dura. Each animal received all the four treatment modalities for Fil- or FilG-based scaffold types. The Fil treatments were labeled Fil040, Fil050, Fil083, and Fil125, and the FilG treatments were labeled FilG040, FilG050, FilG083, and FilG125. Four weeks after the operation, the rabbits received general anesthesia and were sacrificed by an overdose of pentobarbital to harvest the samples for methacrylate embedding[2].

2.3. Histomorphometry

The image analysis software (Image-Pro Plus®; Media Cybernetic, Silver Springs, MD) was used to evaluate the ground section of each sample from the middle of each implant. The area of interest (AOI) was limited by the defect margins, which were 6 mm apart, and the area fraction of the implant submerged into the bony defect. The bony regenerated area is the percentage of bone and bony integrated scaffold in the AOI (bony area, %). Bony bridging, as a measure of osteoconduction, was performed as reported earlier[2,31]. In essence, bone tissue in the AOI as well as bony integrated scaffold is projected onto the *x*-axis. The sum of stretches of the *x*-axis where bone formation had occurred at any level in relation to the defect width (6 mm) yield in bony bridging provided as percentage of defect width.

2.4. Statistics

Statistic was performed as previously reported[2,31]. Values are expressed as mean ± standard deviation or displayed in graphs as median ± lower/upper quartile.

3. Results

3.1. Scaffold library

After debinding and sintering, all scaffolds appeared white to indicate that the yellowish binder was removed during the sinter process. The generation of scaffolds with finer filaments of 0.35 mm failed for the FilG-type arrangement, showing the constrains of our production methodology. In Table 1, the characteristics of all scaffolds are displayed.

The macroporosity and transparency of all scaffolds are identical. For Fil-type scaffolds, all filaments point toward the direction of bone growth; for FilG-type scaffolds, only 50% of the filaments point toward bone growth direction.

The overall design strategy is displayed in Figure 2 as Fil-type and respective FilG-type of identical rod dimension and rod distance are derived from the same microarchitecture (Figure 2A). Directionality of filaments in respect to the advancement of the bone front during the repair of the defect is 100% for the Fil-type scaffolds but only 50% for the FilG-type scaffolds, since in the latter case, 50% of filaments are orthogonal oriented (Figure 2B). Moreover, 3D and 2D

Table 1. Characteristics of all scaffolds from the filament-based library

Microarchitecture	Filaments in direction of bone growth (%)	Rod dimension and rod distance (mm)	Macroporosity (%)	Transparency (%)	Surface of scaffold per mm³ (mm²)	Surface of scaffold per mm³ in direction of bone growth (mm²)
Fil040	100	0.40	50	25	1.87	1.25
FilG040	50	0.40	50	25	1.87	0.62
Fil050	100	0.50	50	25	1.50	1.00
FilG050	50	0.50	50	25	1.50	0.50
Fil083	100	0.83	50	25	0.90	0.59
FilG083	50	0.83	50	25	0.90	0.29
Fil125	100	1.25	50	25	0.60	0.40
FilG125	50	1.25	50	25	0.60	0.20

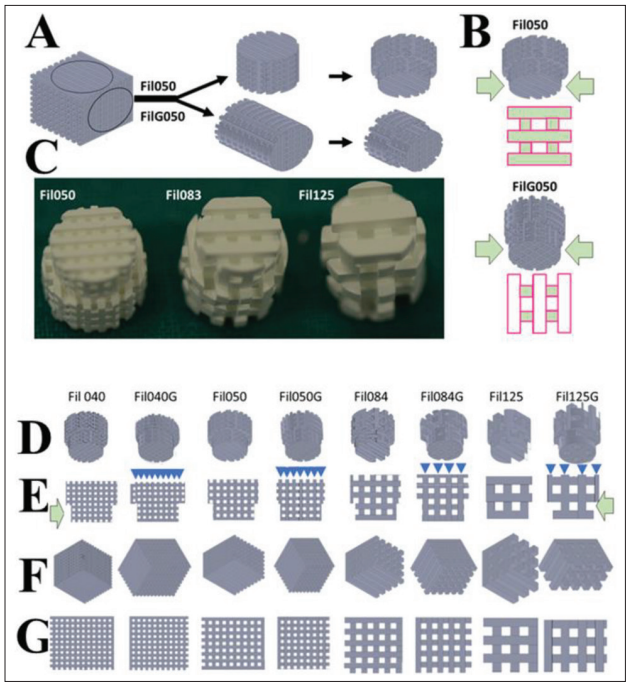

Figure 2. Strategy to generate scaffolds of 100% and 50% directionality from the same microarchitecture. (A) Fil050 and FilG050 are derived from the same microarchitecture. (B) Bone ingrowth direction in the defect (green arrow) is 100% aligned with the filaments for Fil050 (all red circled bares are in green) but only 50% for FilG050 (only 50% of the red-circled bares are in green). (C) Fil-type scaffolds before implantation. The upper part of the scaffolds measures 6 mm in diameter. 3D representations (D) and 2D representations (E) of all constructs and all cubes (F and G) are displayed. The green arrows indicate the bone ingrowth direction. Blue arrows (E) mark the filaments of the constructs orthogonal to the bone ingrowth direction.

pictures are provided for all constructs (Figure 2D and E) and all cubes (Figure 2F and G).

3.2. Osteoconductivity of Fil-type scaffolds

The histologies of the middle sections (Figure 3A) revealed that for implantation over 4 weeks, rod dimension and rod distance had no significant effect on osteoconductivity, which were determined by the degree of defect bridging (Figure 3B).

On average, bony bridging was 91.82 ± 10.84% for Fil040 scaffolds, 84.39 ± 15.85% for Fil050 scaffolds, 92.13 ± 16.65% for Fil083 scaffolds, and 78.64 ± 19.86% for Fil125 scaffolds without any significant difference between the four scaffold types (Figure 3B). Bony regenerated area of Fil040 and Fil050 scaffolds was significantly larger than that of Fil125 scaffolds. The average percentage of bony regenerated area was 79.39 ± 16.43% for Fil040 scaffolds, 69.24 ± 20.27% for Fil050 scaffolds, 63.52 ± 20.99% for Fil083 scaffolds, and 47.95 ± 15.96% for Fil125 scaffolds. Overall, an increase in filament thickness and distance led to a significant decrease in bony regenerated area.

3.3. Osteoconductivity of FilG-type scaffolds

The histologies of the middle sections (Figure 4A) from FilG-type scaffolds with only 50% of the filaments being in line with bone ingrowth direction into the defect revealed that over 4 weeks of implantation, rod dimension and rod distance affected osteoconductivity, determined by the degree of defect bridging significantly (Figure 4B).

On average, bony bridging was 89.91 ± 8.51% for FilG040 scaffolds, 89.98 ± 12.84% for FilG050 scaffolds, 77.85 ± 21.13% for FilG083 scaffolds, and 62.63 ± 27.72% for FilG125 scaffolds. A significant difference was observed between FilG040, FilG050, and FilG125 scaffolds (Figure 4B). Bony bridging with FilG-type scaffolds declined significantly with the increase in filament distance and dimension. The bony regenerated area of FilG040 and FilG050 scaffolds was significantly higher than that of FilG083 and FilG125 scaffolds (Figure 4C). Overall, an increase in filament dimension and distance for FilG-type scaffolds was associated with a decrease in bony regenerated area. The average percentage of bony regenerated area was 67.85 ± 22.45% for FilG040 scaffolds, 69.11 ± 28.93% for FilG050 scaffolds, 47.00 ± 15.34% for Fil083 scaffolds, and 34.30 ± 14.65% for Fil125 scaffolds.

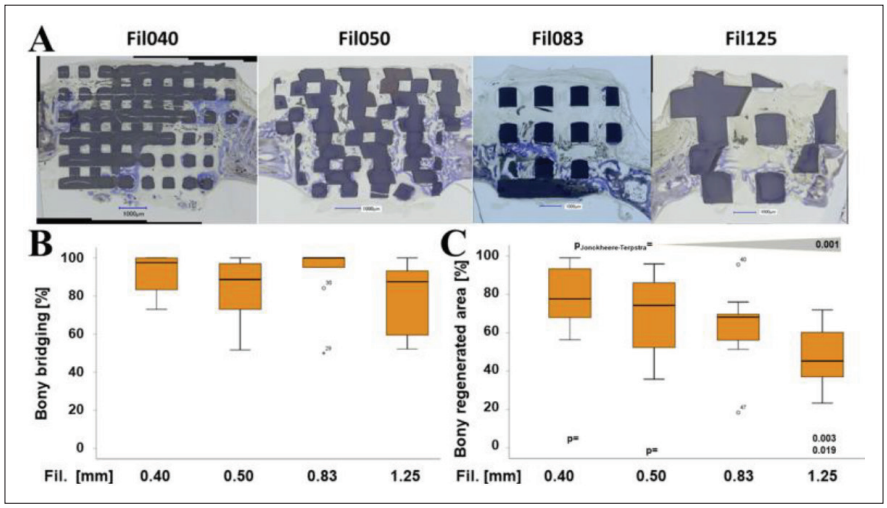

Figure 3. Osteoconduction and bone regeneration from filament-based (Fil-type) microarchitectures. (A) Histological sections from the middle of the noncritical-size defects treated with Fil040, Fil050, Fil083, and Fil125. Histological sections from 4 weeks postoperatively are shown. Scale bars represent 1 mm. Bone (grayish purple to purple) and TCP (grayish) are visualized. Defect bridging (B) and the formation of new bone (C) are displayed.

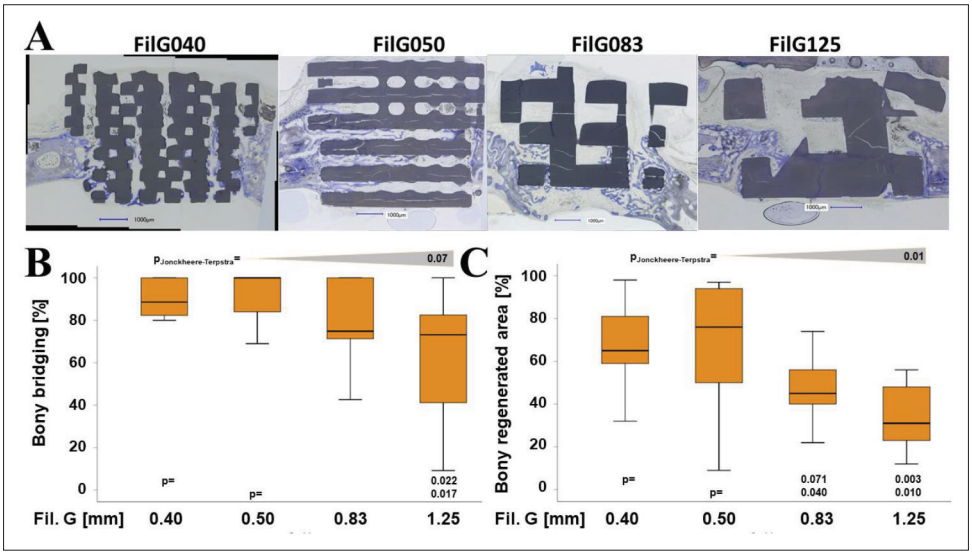

Figure 4. Osteoconduction and bone regeneration from filament G-based (FilG-type) microarchitectures. Histological sections from the middle of the noncritical-size defects treated with FilG040, FilG050, FilG083, and FilG125 (A). Histological sections from 4 weeks postoperatively are shown. Scale bars represent 1 mm. Bone (grayish purple to purple) and TCP (grayish) are visualized. Defect bridging (B) and the formation of new bone (C) are displayed.

4. Discussion

Extrusion-based 3D printing systems are most commonly applied. Therefore, the majority of microarchitectures are composed of filaments[29]. For bone tissue engineering purposes, the optimal filament-based microarchitecture for osteoconduction and bony regeneration is still elusive. In this study, we studied the optimal dimension, distance, and orientation of filaments for osteoconduction and bone regeneration based on a library of scaffolds with filament-based designs. In this library, dimension and distance of filaments spanned 0.40 mm to 1.25 mm. The optimal directionality of filaments was determined with two scaffold types. In the Fil-type scaffolds, 100% of the filaments were in line with the bone front that developed to bridge the defect. In the FilG-type scaffolds, 50% of the filaments were aligned to the bone front while 50% pointed orthogonally to it (Figure 2A and B).

The most interesting result of our study was that with filaments of 0.40 mm to 0.50 mm, high defect bridging values (Figure 5A) and bone regeneration (Figure 5B) were achieved, independently of the direction of the filaments. Nevertheless, the directionality of filaments aligned to bone ingrowth direction is a crucial guiding cue but only comes into play with filaments of 0.83 mm and 1.25 mm.

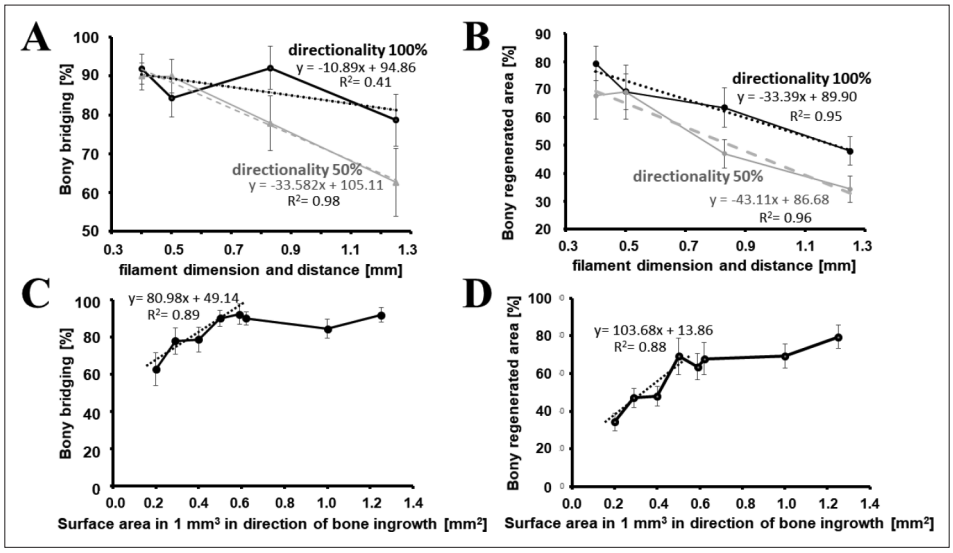

Figure 5. Extent of filament directionality influences osteoconduction and bone regeneration. Correlation of rod dimension/rod distance and directionality on bony bridging (A) and bony regenerated area (B). In (A) and (B), the data set with scaffolds of 100% in direction of bone ingrowth is displayed in black and with 50% directionality in gray. The low R^2 value for directionality of 100% indicates that rod dimension and rod distance have no major influence on bony bridging (black lines), but at 50% directionality (gray lines), an increase in rod dimension and rod thickness is highly associated with a decrease in bony bridging. Correlation of total surface area in direction of bone growth on bony bridging (C) and bony regenerated area (D) are shown.

Filaments beyond 0.83 mm are, therefore, suboptimal for osteoconduction, especially for complex defects where diverse bone fronts from simultaneously. Another crucial aspect of filament-based microarchitectures was found by others[23] in that each second layer of filaments should be aligned in a 0°/90° setting. If only each third layer is aligned as in a 0°/60°/120° filament setting, bone regeneration is compromised. This suggests that it is not only the alignment of the filaments of one layer with the bone front to create a directional space between two adjacent filaments but also an alignment of every second layer of filaments provided in the 0°/90° setting but not in the 0°/60°/120° setting where only each third layer is aligned. In addition, the directional space between two adjacent filaments in one layer has to be complemented by aligned spaces formed by the second filament layers to create an overall osteoconductive space configuration. Although directional bone formation occurs in the space between the filaments and not on their surface[1,32], aligned spaces are defined by aligned surfaces. We found that the area of surface aligned to bone ingrowth per volume is an important determinant of osteoconductivity. A value exceeding 0.5 mm^2 per mm^3 of scaffold is sufficient for this surface to serve as a guiding cue for maximal osteoconductivity. Values below this threshold, however, correlate strongly with a decrease in osteoconductivity (Figure 5C) and bony regeneration (Figure 5D).

The primary criterion for directionality in osteoconduction is defect bridging, since in contrast to bony regenerated area, it reflects a vectorized growth pattern from the defect margins toward the center of the defect. A unilateral vectorized growth pattern is essential for nerve repair[33] and can be generated by a two-photon lithography-based 3D patterning of 200 nm nanofibers. The dimension of these fibers is far below the dimension of the filaments used in this study and resembles the situation for guiding the migration of single cells on a surface[22]. Osteoconduction in wide-open porous scaffolds, however, is guiding bone tissue growth and represents no surface phenomenon since bone formation does not occur predominantly on the surface of the scaffold but between the rods of lattice microarchitectures as shown for two different materials: TCP and titanium[1,32]. Therefore, for osteoconduction, the microarchitecture and to a lesser extent the nanoarchitecture represented by the surface morphology or the microporosity is the dominant determinant as was shown for hydroxyapatite-based 3D-printed scaffolds[34]. For TCP-based scaffolds, surface morphology, and/or microporosity tuned by the sintering temperature affect osteoconductivity[30]. To overcome this possible dependence, all scaffolds of our filament-based library underwent the same post-processing regime to generate a uniform nanoarchitecture in terms of surface morphology and microporosity.

Vascularization is a prerequisite for bone formation and occurs even in pores between 40 and 70 µm. In a set of ceramic scaffolds with pores between 0.04 and 0.28 mm, the density of functional capillaries was the highest with pores exceeding 0.14 mm, and it correlates with the extent of new bone formation[35]. Since the

pores were randomly distributed, directionality was not addressed in that study. The directionality of vascularization is largely hypoxia-driven (low tissue oxygen level), which promotes the sprouting of endothelial cells toward the oxygen-deprived tissue[36,37]. For three different microarchitectures with pores from 0.35 mm to 0.65 mm, blood vessel volume/total volume increased with the pore diameter[38]. In our library, wall distances of 0.40 mm and 0.50 mm yielded the highest degree of osteoconduction and bone regeneration irrespective of directionality of the filaments. One can assume that vascularization is no limiting factor for bone regeneration in wide-open porous microarchitectures as tested in this study and even less so for rod distances of 0.83 mm or 1.25 mm as realized in FilG083 and FilG125 scaffolds, where we saw a significant decline in bone formation compared to the smaller 0.40 mm and 0.50 mm filaments. That suggests that although vascularization is certainly a prerequisite for bone formation and osteoconduction, it is not the limiting factor in wide-open porous microarchitectures.

The optimal pore diameter for osteoconduction was found for TCP-based scaffolds to be between 0.70 and 1.20 mm with bottlenecks between 0.50 and 0.70 mm[13] and optimal rod distance in orthogonal titanium lattice microarchitectures to be 0.80 mm[39]. Here, for TCP-based filament microarchitectures, optimal filament distance for osteoconduction was between 0.40 and 0.83 mm for the Fil-type configuration and between 0.40 and 0.50 mm for the FilG-type configuration. Irrespective of the microarchitecture type, it appears that voids in any microarchitecture should span not more than 0.80 mm to ensure high osteoconductivity and optimal guiding of bone ingrowth. The diagonal of 0.80 mm squares measures 1.13 mm and comes close to the maximal pore size of osteoconductive pore-based microarchitectures of 1.20 mm[1,13]. Despite the high variability of these diverse microarchitectures, based on pores, lattice or filaments, the optimal dimension of the voids between material surfaces is in a range between 0.80 mm and 1.20 mm. Therefore, these numbers can be applied to other microarchitectures as well.

In this study, we used a grid-like configuration of filament microarchitectures based on square-shaped filaments. One could suspect that square-shaped filaments enhance directionality, since they expose directional strait surfaces to the ingrowing bone. To study the effect of round versus square-shape filaments, additional studies on this subject are needed. Moreover, in this study, we only looked at grid-like configurations but also other configuration with wavelike or honeycomb patterns can be produced with extrusion-based 3D printing techniques. Such variations change the mechanics and the *in vitro* outcomes[40], as do double-filament configurations, hollow, core–shell, and bionic filaments[29]. How such new developments will influence scaffold-based bone tissue engineering will be seen over the next decade.

5. Conclusions

In conclusion, we showed that for filament-based microarchitectures, the directionality of filaments, which is a guiding cue for osteoconduction, is a key factor for filament distance of 0.83 mm and beyond. At a distance of 0.40 mm and 0.50 mm, directionality of filaments imposes no major influence on osteoconductivity. The optimal distance of filaments to support and guide osteoconductivity is between 0.40 and 0.50 mm, given that multiple bone ingrowth fronts will form in complex defect configurations.

Acknowledgments

The authors would like to thank Ana Perez for her assistance with histologies.

Funding

This research was funded by the Swiss National Science Foundation, grant number: 310030_197128 to FEW

Conflict of interest

The authors declare no conflicts of interest.

Author contributions

Conceptualization: Franz E. Weber
Methodology: Chafik Ghayor, Indranil Bhattacharya, Julien Guerrero, Franz E. Weber
Formal analysis: Chafik Ghayor, Indranil Bhattacharya, Julien Guerrero, Franz E. Weber
Investigation: Chafik Ghayor, Indranil Bhattacharya, Julien Guerrero, Franz E. Weber
Resources: Franz E. Weber
Data curation: Chafik Ghayor, Indranil Bhattacharya, Julien Guerrero, Franz E. Weber
Writing—original draft preparation: Franz E. Weber
Writing—review and editing: Chafik Ghayor, Indranil Bhattacharya, Julien Guerrero, Franz E. Weber
Visualization: Chafik Ghayor, Indranil Bhattacharya, Franz E. Weber
Supervision: Franz E. Weber
Funding acquisition: Franz E. Weber

Ethics approval and consent to participate

The protocol was in line with the European Union Directive 2010/63/EU and accepted by the local authorities (065/2018).

Consent for publication

Not applicable.

Availability of data

Data are available after finalization of this project upon request to FEW via franz.weber@zzm.uzh.ch.

References

1. Weber FE, 2019, Reconsidering osteoconduction in the era of additive manufacturing. *Tissue Eng Part B Rev*, 25(5): 375–386.

   https://doi.org/10.1089/ten.TEB.2019.0047

2. de Wild M, Schumacher R, Mayer K, *et al.*, 2013, Bone regeneration by the osteoconductivity of porous titanium implants manufactured by selective laser melting: A histological and micro computed tomography study in the rabbit. *Tissue Eng Part A*, 19(23–24): 2645–2654.

   https://doi.org/10.1089/ten.TEA.2012.0753

3. Sears NA, Seshadri DR, Dhavalikar PS, *et al.*, 2016, A review of three-dimensional printing in tissue engineering. *Tissue Eng Part B Rev*, 22(4): 298–310.

   https://doi.org/10.1089/ten.TEB.2015.0464

4. Brunello G, Sivolella S, Meneghello R, *et al.*, 2016, Powder-based 3D printing for bone tissue engineering. *Biotechnol Adv*, 34(5): 740–753.

   https://doi.org/10.1016/j.biotechadv.2016.03.009

5. Sachs E, Cima M, Cornie J, 1990, Three-dimensional printing: Rapid tooling and prototypes directly from a CAD model. *CIRP Ann Manuf Technol*, 39(1): 201–204.

   http://dx.doi.org/10.1016/S0007-8506(07)61035-X

6. Butscher A, Bohner M, Doebelin N, *et al.*, 2013, New depowdering-friendly designs for three-dimensional printing of calcium phosphate bone substitutes. *Acta Biomater*, 9(11): 9149–9158.

   http://dx.doi.org/10.1016/j.actbio.2013.07.019

7. Butscher A, Bohner M, Roth C, *et al.*, 2012, Printability of calcium phosphate powders for three-dimensional printing of tissue engineering scaffolds. *Acta Biomater*, 8: 373–385.

8. Karageorgiou V, Kaplan D, 2005, Porosity of 3D biomaterial scaffolds and osteogenesis. *Biomaterials*, 26(27): 5474–5491.

   https://doi.org/10.1016/j.biomaterials.2005.02.002

9. Kuboki Y, Jin Q, Takita H, 2001, Geometry of carriers controlling phenotypic expression in BMP-induced osteogenesis and chondrogenesis. *J Bone Joint Surg (Am Vol)*, 83-A Suppl 1(Pt 2): S105–S115.

10. Kuboki Y, Takita H, Kobayashi D, *et al.*, 1998, BMP-induced osteogenesis on the surface of hydroxyapatite with geometrically feasible and nonfeasible structures: Topology of osteogenesis. *J Biomed Mater Res*, 39(2): 190–199.

11. Tsuruga E, Takita H, Itoh H, *et al.*, 1997, Pore size of porous hydroxyapatite as the cell-substratum controls BMP-induced osteogenesis. *J Biochem*, 121(2): 317–324.

12. von Doernberg M-C, von Rechenberg B, Bohner M, *et al.*, 2006, In vivo behavior of calcium phosphate scaffolds with four different pore sizes. *Biomaterials*, 27(30): 5186–5198.

    http://dx.doi.org/10.1016/j.biomaterials.2006.05.051

13. Ghayor C, Weber FE, 2018, Osteoconductive microarchitecture of bone substitutes for bone regeneration revisited. *Front Physiol*, 9: 960.

    https://doi.org/10.3389/fphys.2018.00960

14. Cornell CN, Lane JM, 1998, Current understanding of osteoconduction in bone regeneration. *Clin Orthop Relat Res*, 355: S267–S273.

15. Urist MR, 1976, Practical applications of basic research on bone graft physiology. *The American Academy of Orthopaedic Surgeons: Instructional Course Lectures*, Vol XXV, The C.V. Mosby Company, St Louis, 1–26.

16. Li J, Liu Y, Zhang Y, *et al.*, 2021, Biophysical and biochemical cues of biomaterials guide mesenchymal stem cell behaviors. *Front Cell Dev Biol*, 9: 640388.

    https://doi.org/10.3389/fcell.2021.640388

17. Horwitz R, Webb D, 2003, Cell migration. *Curr Biol*, 13(19): R756–R759.

    https://doi.org/10.1016/j.cub.2003.09.014

18. Mayor R, Etienne-Manneville S, 2016, The front and rear of collective cell migration. *Nat Rev Mol Cell Biol*, 17(2): 97–109.

    https://doi.org/10.1038/nrm.2015.14

19. Schwartz MA, Horwitz AR, 2006, Integrating adhesion, protrusion, and contraction during cell migration. *Cell*, 125(7): 1223–1225.

    https://doi.org/10.1016/j.cell.2006.06.015

20. Qian T, Wang Y, 2010, Micro/nano-fabrication technologies for cell biology. *Med Biol Eng Comput*, 48(10): 1023–1032.

    https://doi.org/10.1007/s11517-010-0632-z

21. Diloksumpan P, Bolaños RV, Cokelaere S, *et al.*, 2020, Orthotopic bone regeneration within 3D printed bioceramic scaffolds with region-dependent porosity gradients in an equine model. *Adv Healthc Mater*, 9(10): 1901807.

    https://doi.org/10.1002/adhm.201901807

22. Xue J, Wu T, Xia Y, 2018, Perspective: Aligned arrays of electrospun nanofibers for directing cell migration. *APL Mater*, 6(12): 120902.

    https://doi.org/10.1063/1.5058083

23. Berner A, Woodruff MA, Lam CX, *et al.*, 2014, Effects of scaffold architecture on cranial bone healing. *Int J Oral Maxillofac Surg*, 43(4): 506–513.

    https://doi.org/10.1016/j.ijom.2013.05.008

24. Crump SS, 1992, Apparatus und method for creating tree-dimensional objects. *Patent*, No. 5121329.

25. Millán AJ, Santacruz I, Sánchez-Herencia AJ, *et al.*, 2002, Gel-extrusion: A new continuous forming technique. *Adv Eng Mater*, 4(12): 913–915.

    https://doi.org/10.1002/adem.200290002

26. Vozzi G, Previti A, De Rossi D, *et al.*, 2002, Microsyringe-based deposition of two-dimensional and three-dimensional polymer scaffolds with a well-defined geometry for application to tissue engineering. *Tissue Eng*, 8(6): 1089–1098.

    https://doi.org/10.1089/107632702320934182

27. Hutmacher DW, Schantz T, Zein I, *et al.*, 2001, Mechanical properties and cell cultural response of polycaprolactone scaffolds designed and fabricated via fused deposition modeling. *J Biomed Mater Res*, 55: 203–216.

28. Schantz JT, Lim TC, Ning C, *et al.*, 2006, Cranioplasty after trephination using a novel biodegradable burr hole cover: Technical case report. *Neurosurgery*, 58(1 Suppl): ONS-E176; discussion ONS-E176.

    https://doi.org/10.1227/01.NEU.0000193533.54580.3F

29. Lin C, Wang Y, Huang Z, *et al.*, 2021, Advances in filament structure of 3D bioprinted biodegradable bone repair scaffolds. *Int J Bioprint [Internet]*, 7(4): 426.

    https://doi.org/10.18063/ijb.v7i4.426

30. Ghayor C, Chen TH, Bhattacharya I, *et al.*, 2020, Microporosities in 3D-printed tricalcium-phosphate-based bone substitutes enhance osteoconduction and affect osteoclastic resorption. *Int J Mol Sci*, 21(23): 9270.

    https://doi.org/10.3390/ijms21239270

31. de Wild M, Zimmermann S, Ruegg J, *et al.*, 2016, Influence of microarchitecture on osteoconduction and mechanics of porous titanium scaffolds generated by selective laser melting. *3d Print Addit Manuf*, 3(3): 142–151.

    https://doi.org/10.1089/3dp.2016.0004

32. Chen TH, Ghayor C, Siegenthaler B, *et al.*, 2018, Lattice microarchitecture for bone tissue engineering from calcium phosphate compared to titanium. *Tissue Eng Part A*, 24(19–20): 1554–1561.

    https://doi.org/10.1089/ten.TEA.2018.0014

33. Agrawal L, Saidani M, Guillaud L, *et al.*, 2021, Development of 3D culture scaffolds for directional neuronal growth using 2-photon lithography. *Mater Sci Eng C*, 131: 112502.

    https://doi.org/10.1016/j.msec.2021.112502

34. Ghayor C, Bhattacharya I, Guerrero J, *et al.*, 2022, 3D-printed HA-based scaffolds for bone regeneration: Microporosity, osteoconduction and osteoclastic resorption. *Materials*, 15(4): 1433.

35. Klenke FM, Liu Y, Yuan H, *et al.*, 2008, Impact of pore size on the vascularization and osseointegration of ceramic bone substitutes in vivo. *J Biomed Mater Res A*, 85(3): 777–786.

    https://doi.org/10.1002/jbm.a.31559

36. Mastrullo V, Cathery W, Velliou E, *et al.*, 2020, Angiogenesis in tissue engineering: As nature intended? *Front Bioeng Biotechnol*, 8: 188.

    https://doi.org/10.3389/fbioe.2020.00188

37. Yang G, Mahadik B, Choi JY, *et al.*, 2020, Vascularization in tissue engineering: Fundamentals and state-of-art. *Prog Biomed Eng (Bristol)*, 2(1): 012002.

    https://doi.org/10.1088/2516-1091/ab5637

38. Wu F, Yang J, Ke X, *et al.*, 2022, Integrating pore architectures to evaluate vascularization efficacy in silicate-based bioceramic scaffolds. *Regen Biomater [Internet]*. 9: rbab077.

    https://doi.org/10.1093/rb/rbab077

39. de Wild M, Ghayor C, Zimmermann S, *et al.*, 2019, Osteoconductive lattice microarchitecture for optimized bone regeneration. *3D Print Addit Manuf*, 6(1): 40–49.

    https://doi.org/10.1089/3dp.2017.0129

40. Huber F, Vollmer D, Vinke J, *et al.*, 2022, Influence of 3D printing parameters on the mechanical stability of PCL scaffolds and the proliferation behavior of bone cells. *Materials (Basel, Switzerland) [Internet]*. 15(6): 2091.

    https://doi.org/10.3390/ma15062091